

High-Temperature Annealing Induced He Bubble Evolution in Low Energy He Ion Implanted 6H-SiC *

Yu-Zhu Liu(刘玉柱)¹, Bing-Sheng Li(李炳生)^{2**}, Li Zhang(张莉)³

¹Jiangsu Collaborative Innovation Center on Atmospheric Environment and Equipment Technology (CICAEET),
Nanjing University of Information Science & Technology,
Nanjing 210044

²Institute of Modern Physics, Chinese Academy of Sciences, Lanzhou 730000

³Department of Physics, School of Science, Lanzhou University of Technology, Lanzhou 730050

(Received 14 January 2017)

Bubble evolution in low energy and high dose He-implanted 6H-SiC upon thermal annealing is studied. The (0001)-oriented 6H-SiC wafers are implanted with 15 keV helium ions at a dose of $1 \times 10^{17} \text{ cm}^{-2}$ at room temperature. The samples with post-implantation are annealed at temperatures of 1073, 1173, 1273, and 1473 K for 30 min. He bubbles in the wafers are examined via cross-sectional transmission electron microscopy (XTEM) analysis. The results present that nanoscale bubbles are almost homogeneously distributed in the damaged layer of the as-implanted sample, and no significant change is observed in the He-implanted sample after 1073 K annealing. Upon 1193 K annealing, almost full recrystallization of He-implantation-induced amorphization in 6H-SiC is observed. In addition, the diameters of He bubbles increase obviously. With continually increasing temperatures to 1273 K and 1473 K, the diameters of He bubbles increase and the number density of lattice defects decreases. The growth of He bubbles after high temperature annealing abides by the Ostwald ripening mechanism. The mean diameter of He bubbles located at depths of 120–135 nm as a function of annealing temperature is fitted in terms of a thermal activated process which yields an activation energy of $1.914 \pm 0.236 \text{ eV}$.

PACS: 28.41.Qb, 61.80.Jh, 61.82.Fk, 81.40.Wx

DOI: 10.1088/0256-307X/34/5/052801

Due to its excellent physical, electronic and optical properties, great efforts have been taken to exploring the potential of silicon carbide (SiC) for the development of high-temperature, high-power, high-frequency electronic devices as well as for structural components in nuclear energy and waste technologies due to a low cross-section for neutron capture and its excellent structural, chemical and mechanical stability.^[1–3] Energetic He atoms can be formed through nuclear reactions within SiC and will accumulate and cause degradation of material properties. However, in semiconductor technology, it has been shown that He implantation-induced cavities can effectively trap metallic impurities in SiC, to satisfy the requirements for the future development of microelectronic devices.^[4] The cavities can trap self-interstitials to inhibit the transient enhanced diffusion.^[5] In parallel, the microcavities that coalesce through the entire substrate can transfer one entire layer to another substrate to enable the fabrication of SiC-on-insulator (SiCOI) structures.^[6] Deep level transient spectroscopy measurements have reported that cavities present deep levels localized near the middle of band gaps. Therefore, these cavities can also be used for the generation of recombination centers to control the charge carrier lifetime in the active region of SiC power devices.^[7] In silicon, recent studies have reported that cavities can effectively trap oxygen and self-interstitials to enable the fabrication of SOI structures with low lattice defects compared with those obtained through separation by implanted oxygen.^[8–10] It may be a similar phenomenon for fabricating SiCOI structures via helium and oxygen co-implantation into SiC. The understanding of He implantation effects in SiC is therefore

of primary importance. The irradiation-induced bubbles evolve into cavities due to gas desorption under annealing and lattice defects of He-irradiated SiC have been extensively investigated. Zhang *et al.* studied the relation of implantation temperature and threshold dose for forming nanoscale bubbles.^[11] The dose threshold is about 0.35 at.% of the He-concentration peak for room-temperature (RT) implantation, and it increases to a value from 1.5 to 2.7 at.% of He-concentration peak for 500 K implantation. Beaufort *et al.* investigated the distribution of the cavities in 1.6 MeV He-implanted 4H-SiC at a dose of $5 \times 10^{16} \text{ cm}^{-2}$ at RT followed by 1773 K annealing.^[12] Three different zones can be distinguished. They observed a low density of cylindrical cavities lying on the basal plane in front of the He implantation-induced amorphization zone. The largest cavities are located at a depth between the He damage peak and the He concentration peak. A high density of faceted cavities is located in back of the He implantation-induced amorphization zone. Increasing dose to $1 \times 10^{17} \text{ cm}^{-2}$, circular and faceted bubbles are formed in the middle of the damaged band.^[13] However, Zhang *et al.* investigated the distribution of He-implantation-induced bubbles in the 30 keV He-implanted 4H-SiC at a dose of $2 \times 10^{17} \text{ cm}^{-2}$ at 500 K followed by 1173 K annealing.^[10] There are larger planar clusters of bubbles at both boundaries of the bubble layer and smaller spherical bubbles in the middle of the bubble layer. Barbot *et al.* observed bubbles with 1–2 nm in diameter homogeneously distributed in the damaged band of the 50 keV He-implanted 4H-SiC at a dose of $1 \times 10^{17} \text{ cm}^{-2}$ at 973 K in the as-implanted state.^[12] Upon 1773 K annealing, initial nanoscale spherical bubbles evolve into large rectangular paralle-

*Supported by the National Natural Science Foundation of China under Grant No 11475229.

**Corresponding author. Email: b.s.li@impcas.ac.cn

© 2017 Chinese Physical Society and IOP Publishing Ltd

lepipied cavities with facets parallel and perpendicular to the surface. Numerous studies have been devoted to He implantation with energy ranging from tens of keV to MeV into SiC for the study on bubble formation.^[11–14] Few studies related to low energy He implantation, nevertheless, low energy implantation is well suited for the application of semiconductor technologies. In the present work, the formation and evolution of He bubbles in 15 keV He-implanted 6H-SiC have been studied as a function of the subsequent annealing temperature. Using both conventional transmission electron microscopy (CTEM) and high resolution TEM (HRTEM) the bubble distribution after recrystallization has been observed.

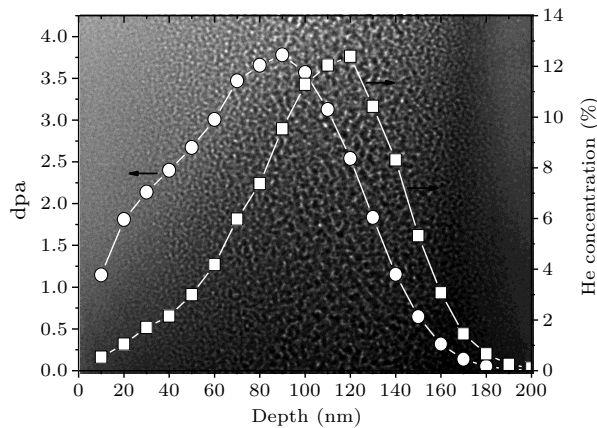


Fig. 1. The distributions of lattice damage in units of dpa and the deposited concentration of He in 6H-SiC implanted with 15 keV He ions at a dose of $1 \times 10^{17} \text{ cm}^{-2}$, overlaid on the corresponding XTEM bright-field micrograph of the as-implanted 6H-SiC sample.

The 6H-SiC wafer oriented $\langle 0001 \rangle_{\text{Si}}$ surface with 0.3 mm thickness supplied by the MIT company was implanted by 15 keV He ions at a dose of $1 \times 10^{17} \text{ cm}^{-2}$ with a current density of approximately $1.0 \mu\text{A cm}^{-2}$. The sample holder was kept at RT during He implantation. The implantation damage in displacements per atom (dpa) and concentration were simulated by SRIM-2008 (using C and Si sublattice displacement energies of 20 and 35 eV, respectively, and density of 3.21 g cm^{-3}).^[15] The results are shown in Fig. 1. The mean projected range R_p is about 115 nm with a straggling of ΔR_p to be about 75 nm. The He-concentration peak is 12% and the damage peak is over 3.5 dpa. The implantation experiment was performed in the 320 kV multi-discipline research platform for highly charged ions of the Institute of Modern Physics, Chinese Academy of Sciences (CAS). Post-implantation, the wafer was cut into several pieces and then isochronally annealed in a tube furnace at temperatures of 1073, 1173, 1273 and 1473 K for 30 min in a vacuum.

Microstructural evolution of the He-implanted 6H-SiC upon annealing was investigated via TEM using a Tecnai G20 operated at 200 kV and was equipped with a double tilt goniometer stage. The fabrication process of cross-sectional TEM (XTEM) samples has been described in our previous report.^[16] The bubbles were imaged in under-focused and over-focused conditions to highlight the bubble edges with the Fresnel

contrast.

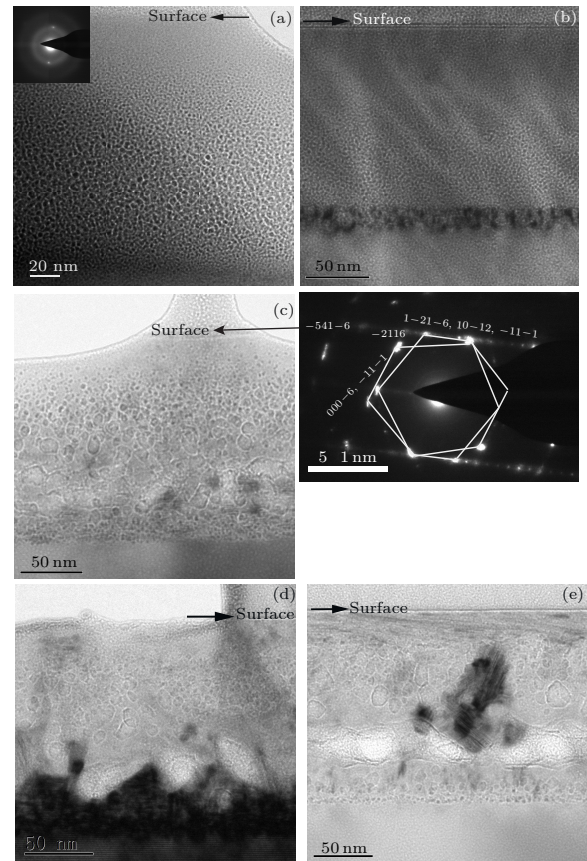


Fig. 2. Over-focus XTEM bright-field micrographs of 6H-SiC implanted with 15 keV He ions at a dose of $1 \times 10^{17} \text{ cm}^{-2}$ at RT: (a) as-implanted state, after annealing at (b) 1073 K, (c) 1173 K, (d) 1273 K, and (e) 1473 K for 30 min. The electron diffraction patterns of the damaged layer before and after annealing at 1173 K are shown in the insets of (a) and (c), respectively.

Figure 1 presents a contrasting region with a width of approximately 180 nm centered at a depth of approximately 110 nm. It is located at the depth region between the maximum He-induced displacement and the maximum He deposition as simulated using SRIM-2008. There are dense bubbles with 1–2 nm in diameter located in the inner amorphous zone, as verified by selected area electron diffraction (inset of Fig. 2(a)). The over-focused bright-field XTEM images presented in Figs. 2(a)–2(e) depict the bubbles in the damage zone of He-implanted 6H-SiC, as-implanted state, after annealing at 1073 K, 1173 K, 1273 K and 1473 K, respectively. To investigate the bubble formation in the damage zone, the depth and diameter distributions of the He bubbles for all five conditions are plotted in Fig. 3. In the as-implanted sample (see Figs. 3(a) and 3(b)), numerous He bubbles are distributed from 20 nm in depth to 180 nm into the bulk. The bubbles are spherical in shape and are almost homogeneously distributed. The mean diameter of observed nanoscale bubbles at the depth distribution range from 1.5 to 2 nm and the majority of the bubbles have diameters of 1.4–1.8 nm. In the near surface zone, no bubbles can be observed. After annealing at 1073 K (see Figs. 3(c) and 3(d)), the mean diameter and distribution of the bubbles are similar to the case of the

as-implanted sample. After annealing at 1173 K, the diameters of the bubbles have changed significantly, as shown in Figs. 3(d) and 3(e). The diameter and number density of the bubbles are inhomogeneously distributed. He bubbles are distributed from 30 nm in depth to 150 nm into the bulk and the mean diameters of the bubbles have a range of 2–7 nm. The mean diameters of the bubbles with depth present a Gaussian-like distribution. The minimum diameter of the bubbles is located at both boundaries of the bubble layer. The maximum diameter of the bubbles is located at the depth of 100 nm. In addition, there is a high number density of the bubbles located at the end of the projected range. The selected area electron diffraction proves the recrystallization of the damaged layer after 1173 K annealing (inset of Fig. 2(c)). The electron diffraction pattern shows two different diffraction patterns, which are $[1\bar{2}10]$ and $[011]$, as indicated in the inset of Fig. 2(c). The present electron diffraction result demonstrates that the polycrystalline structure has been formed, including 3C-SiC structure and epitaxial 6H-SiC. After annealing at 1273 K, the He bubble distribution is similar to the case of the He-implanted sample after 1173 K annealing. He bubbles are distributed from 30 nm in depth to 150 nm into the bulk, and the mean diameters of the bubbles have a range of 3–8 nm. After annealing at 1473 K, the He bubble distribution is also similar to the case of the He-implanted sample after 1173 K annealing. He bubbles are distributed from 30 nm in depth to 160 nm into the bulk, and the mean diameters of observed bubbles have a range of 4–22 nm. The width of the bubble layer increases due to the significant lattice swelling in the He-implanted sample after 1473 K annealing. As shown in Figs. 2(c)–2(e), a high density and small diameter of observed bubbles are located at the lower boundary of the bubble layer, which corresponds to the end of the projected range. Moreover, a low density and large diameter of observed bubbles are located at depth range from 120 to 135 nm, corresponding to the location of the maximum He deposition.

The present experimental results show that a high density of small and spherical bubbles are located in both boundaries of the bubble layer, and a low density of large and faceted bubbles are located in the inner of the bubble layer. It indicates that the bubble growth can be described by the Ostwald ripening mechanism. The growth of observed bubbles after isochronal annealing can be written in the form^[17]

$$\ln[T(r_{\text{mean}}^2)] = -E_a/kT.$$

Figure 4(a) shows the result of the growth of observed bubbles located in the depth range from 120 to 135 nm after isochronal annealing. The slope of the straight line provides an estimate of the activation energy for the growth of the He bubbles, which is 1.914 ± 0.236 eV, as shown in Fig. 4(b). Since the present experimental results have shown that the thermal evolution of the bubbles is followed by an Ostwald ripening mechanism, the obtained activation energy is related to the vacancy migration energy needed by the diffusion from one small bubble to the large one. Weber *et al.* reported an activation energy of 2.2–2.35 eV for the migration of Si-vacancy in SiC. The

present experimental result is lower.^[18] It can be related to strong lattice tensile strains introduced by He bubbles and extended defects in the region of the bubble layer. Density functional theory simulation proved that vacancy-type defects migration can be enhanced in the tensile strain surrounding.^[19]

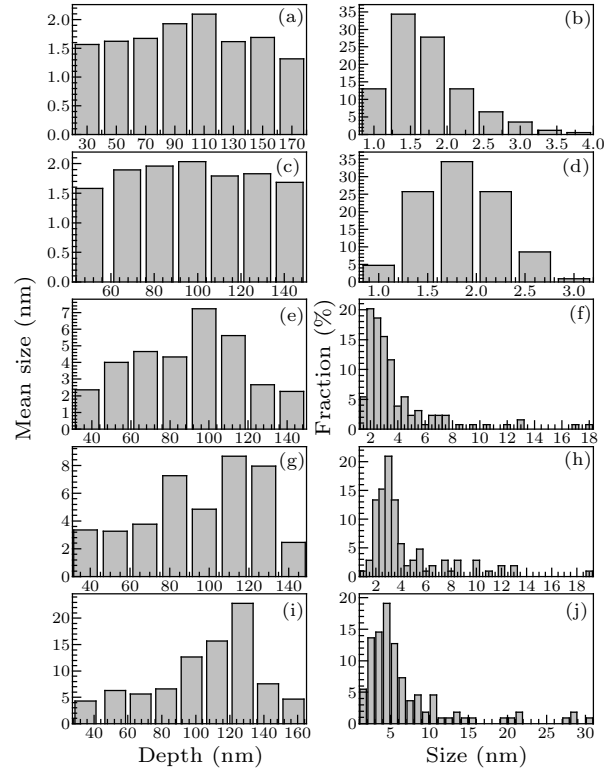


Fig. 3. (a), (c), (e), (g), (i) Bubble depth and (b), (d), (f), (h), (j) bubble diameter distributions for 15 keV He⁺-implanted 6H-SiC at RT: [(a), (b)] as-implanted state, after annealing at [(c), (d)] 1073 K, [(e), (f)] 1173 K, [(g), (h)] 1273 K, and [(i), (j)] 1473 K for 30 min.

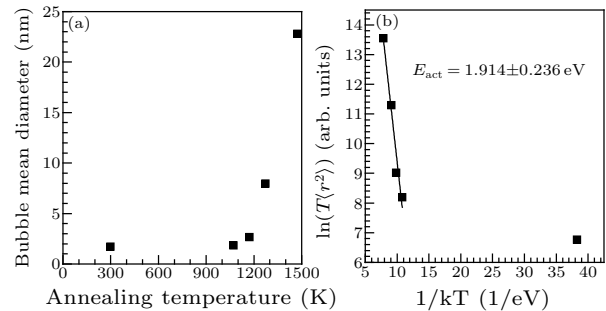


Fig. 4. (a) Variation of the mean diameter of bubbles in the depth of 120–135 nm as a function of the annealing temperature, and (b) measurement of the activation energy of bubble growth.

The bubble layer was investigated by HRTEM. In the near surface region, the bubble exhibits a round shape with nanoscale as shown in Fig. 5(a). The image is the Fourier filtered image with the (1102) spot, as shown in Fig. 5(b). In the periphery of the bubble, basal dislocation loops and prismatic dislocation loops are observed. In the middle of the damaged layer, the large three-dimensional bubbles are faceted along $\{0001\}$ and $\{1\bar{1}00\}$ planes and are as large as 20 nm. The formation of faceted bubbles is due to the coalescence of adjoining helium bubbles, as shown in

Fig. 5(c). In the periphery of the bubble, lattice fringes are significantly disordered. Some regions show the Moire fringes as indicated by arrows in Fig. 5(c). The presence of the Moire fringe is due to the coexistence of 6H-SiC and 3C-SiC in this region. The formation of 3C-SiC in amorphous 6H-SiC after high temperature annealing has been widely reported.^[20,21] The Fourier transform pattern illustrates a polycrystalline structure in this region, as shown in the inset of Fig. 2(c). The mismatch of lattice constant between 6H-SiC and 3C-SiC, as well as the growth of the faceted bubbles followed by emitting self-interstitials, induce a higher density of lattice defects that are observed in the bubble layer. Compared with the relative clear lattice fringes shown in the near surface region, the lattice fringes are vague in the middle of the damaged layer. In the end of the damaged layer, lattice fringes are clearly observed, as shown in Fig. 5(d). Lattice fringes are wavy, indicating a high density of stacking faults and dislocation loops in this region. For example, the zigzag pattern of a normal stacking sequence is symbolized as ...3/3/3/3.... On the left-hand side of the arrowhead shown in the inset of Fig. 5(d), the zigzag pattern is locally changed to ...3/3/4/1/3, which is related to the stacking fault. It has been confirmed that the extra Si-C bilayer inserted parallel to the basal plane of 6H-SiC can form this stacking fault. The Fourier transformation pattern shown in the inset of Fig. 5(d) demonstrates the same lattice structure and orientation as the substrate, indicating the epitaxial 6H-SiC layer-by-layer grown from the substrate.

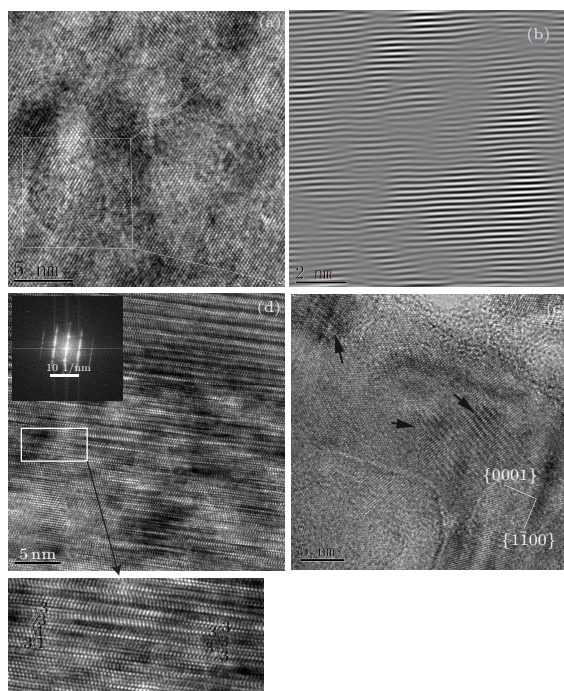


Fig. 5. (a) HRTEM image showing bubbles formed in the near surface region of the He⁺-implanted 6H-SiC after 1173 K annealing as well as (b) the corresponding Fourier filtered image with the (-1102) spot. (c) HRTEM image showing bubbles formed in the inner of the damaged layer as well as (d) stacking faults formed in the end of the damaged layer.

In summary, we have investigated the bubble

evolution of 15 keV He-implanted 6H-SiC at a dose of $1 \times 10^{17} \text{ cm}^{-2}$ followed by annealing ranging from 1073 K to 1473 K for 30 min in a vacuum. Nanoscale bubbles with 1–2 nm are homogeneously distributed in the amorphous layer of the as-implanted sample. Bubbles do not grow after 1073 K annealing, while their diameters increase significantly after 1173 K annealing, corresponding to substantial recrystallization of the amorphous layer. The diameters of the bubbles increase with increasing annealing temperatures from 1173 K to 1473 K. The distribution of bubbles is inhomogeneous, a high density of spherical bubbles located in both boundaries of the bubble layer, and a low density of large and faceted bubbles located in the inner of the bubble layer. The growth of He bubbles after high temperature annealing abides by the Ostwald Ripening mechanism, which yields an activation energy of $1.914 \pm 0.236 \text{ eV}$.

We appreciate the Laboratory of 320 kV High-Voltage Platform in the Institute of Modern Physics, CAS for the helium implantation. In addition, we would like to thank Li-Jun Xu for the XTEM measurement.

References

- [1] Snead L L, Nozawa T, Katoh Y, Byun T S, Kondo S and Petti D A 2007 *J. Nucl. Mater.* **371** 329
- [2] Snead L L, Katoh Y, Henager C H, Hasegawa A, Kohyama A and Riccardi B 2007 *J. Nucl. Mater.* **367** 659
- [3] Katoh Y, Kohyama A, Nozawa T and Sato M 2004 *J. Nucl. Mater.* **329** 587
- [4] Kazan M, Ottaviani L, Moussaed E, Nader R and Masri P 2008 *J. Appl. Phys.* **103** 053707
- [5] Boninelli S, Claverie A, Impellizzeri G, Mirabella S, Priolo F, Napolitani E and Cristiano F 2006 *Appl. Phys. Lett.* **89** 171916
- [6] Tong Q Y, Lee T H, Werner P, Gösele U, Bergmann R B and Werner J H 1997 *J. Electrochem. Soc.* **144** L111
- [7] Rainieri V, Fallica P G and Libertio S 1996 *J. Appl. Phys.* **79** 9012
- [8] Ou X, Kögler R, Mücklich A, Skorupa W, Möller W, Wang X and Vines L 2009 *Appl. Phys. Lett.* **94** 011903
- [9] Li B S, Zhang C H, Zhou L H and Yang Y T 2008 *Chin. Phys. Lett.* **25** 3720
- [10] Li B S, Zhang C H, Zhang H H, Zhang Y, Yang Y T and Zhang L Q 2011 *Nucl. Instrum. Methods Phys. Res. Sect. B* **269** 739
- [11] Zhang C H, Donnelly S E, Vishnyakov V M and Evans J H 2003 *J. Appl. Phys.* **94** 6017
- [12] Beaufort M F, Pailloux F, Declémy A and Barbot J F 2003 *J. Appl. Phys.* **94** 7116
- [13] Oliviero E, David M L, Beaufort M F, Nomgaudyte J, Pranivicius L and Declémy A B J F 2002 *J. Appl. Phys.* **91** 1179
- [14] Li B S, Zhang C H, Zhang H H, Shibayama T and Yang Y T 2011 *Vacuum* **86** 452
- [15] Zieler J F, Biersack J P and Littmark U 1984 *The Stopping Power and Range of Ions in Solids* (New York: Pergamon Press)
- [16] Li B S and Wang Z G 2015 *J. Phys. D* **48** 225101
- [17] Grisolia J, Cristinano F, De B, Ben G, Letertre F, Aspar B, Di L and Claverie A 2000 *J. Appl. Phys.* **87** 8415
- [18] Weber W J, Gao F, Devanathan R, Jiang W L and Zhang Y W 2004 *Mater. Res. Soc. Symp. Proc.* **792** R5.1.1
- [19] AL-Hamadany R, Goss J P, Briddon P R, Mojarad S A, O'Neill A G and Rayson M J 2013 *J. Appl. Phys.* **113** 224108
- [20] Heine V, Cheng C, Engel G E and Needs R J 1992 *Mater. Res. Soc. Symp. Proc.* **242** 507
- [21] Heera V, Kogler R, Skorupa W and Stoemenos J 1995 *Appl. Phys. Lett.* **67** 1999